ISSN 0036-0236, Russian Journal of Inorganic Chemistry, 2024. © Pleiades Publishing, Ltd., 2024.

PHYSICAL AND CHEMICAL ANALYSIS OF INORGANIC SYSTEMS

Phase Equilibria, Crystal Structures, and Oxygen Nonstoichiometry of Complex Oxides Formed in the $GdCoO_3$–$SrCoO_{3-\delta}$–$SrFeO_{3-\delta}$–$GdFeO_3$ System

T. V. Aksenova[a], *, E. E. Solomakhina[a], A. S. Urusova[a], and V. A. Cherepanov[a]

[a] *Ural Federal University named after the First President of Russia B.N. Yeltsin, Yekaterinburg, 620002 Russia*

**e-mail: TV.Aksenova@urfu.ru*

Received February 10, 2024; revised March 12, 2024; accepted March 21, 2024

Abstract—The phase relationships in the quasi-quaternary system $GdCoO_3$–$SrCoO_{3-\delta}$–$SrFeO_{3-\delta}$–$GdFeO_3$ at 1373 K in air have been studied. The homogeneity ranges and crystal structure of solid solutions with overall composition $Gd_{1-x}Sr_xCo_{1-y}Fe_yO_{3-\delta}$ have been determined. Depending on the concentration of introduced strontium and iron, the $Gd_{1-x}Sr_xCo_{1-y}Fe_yO_{3-\delta}$ oxides crystallize in orthorhombic ($x = 0.1$ and $0.4 \le y \le 1.0$; $x = 0.2$ and $y = 0.9$, space group *Pbnm*), tetragonal ($0.6 \le x \le 0.8$ and $0.1 \le y \le 0.5$, space group *I*4/*mmm*) or cubic ($x = 0.9$ and $0.1 \le y \le 0.9$; $0.6 \le x \le 0.8$ and $0.6 \le y \le 0.9$, space group $Pm\bar{3}m$) perovskite structure. Structural parameters were determined for all single-phase samples. It was found that an increase in the concentration of strontium and iron leads to an increase in the unit cells parameters of the $Gd_{1-x}Sr_xCo_{1-y}Fe_yO_{3-\delta}$ oxides. It has been shown that the oxygen content in the $Gd_{1-x}Sr_xCo_{0.3}Fe_{0.7}O_{3-\delta}$ oxides, determined by thermogravimetric analysis, decreases with increasing temperature and strontium content. An isobaric-isothermal phase diagram for the $GdCoO_3$–$SrCoO_{3-\delta}$–$SrFeO_{3-\delta}$–$GdFeO_3$ system at 1373 K in air was constructed.

Keywords: complex oxides, X-ray diffraction, crystal structure, thermogravimetric analysis, oxygen nonstoichiometry, phase diagram

DOI: 10.1134/S0036023624601090

INTRODUCTION

The set of interesting physicochemical characteristics of complex oxides with a perovskite structure, in which rare earth and alkaline earth elements are located in the A-sites, and cobalt and iron in the B-sites [1–5], open up prospects for their practical use in a variety of electrochemical and catalytic devices. The study of the crystal structure and physicochemical properties of strontium-substituted cobaltites $Ln_{1-x}Sr_xCoO_{3-\delta}$ (Ln = REE) was undertaken due to the possibility of their practical use as cathodes [6–12] or interconnectors [13] for intermediate-temperature solid oxide fuel cells (SOFCs), cathodes of CO_2 lasers [14], catalysts [15–17], gas-sensitive sensors [16, 18, 19], materials for chemical looping [20], thermoelectrics [21], magnetic materials [22–25].

Depending on the radius of the lanthanide ion, the concentration of introduced strontium, and the heat treatment conditions, the $Ln_{1-x}Sr_xCoO_{3-\delta}$ oxides can crystallize in the rhombohedral (Ln = La with $0.0 \le x \le 0.5$, space group $R\bar{3}c$) [26–29], orthorhombic (Ln = Pr, Nd, Sm with $0.0 \le x \le 0.6$ and Ln = Gd with $0.37 \le x \le 0.6$ space group *Pbnm* or *Pnma*) [8, 26, 30–32] or cubic Ln = La with $0.6 \le x \le 0.8$ (space group $Pm\bar{3}m$) [28, 29] perovskite structure. Cobaltites $Ln_{1-x}Sr_xCoO_{3-\delta}$ enriched with strontium $0.6 < x < 0.9$ are characterized by structural ordering of lanthanide and strontium ions in the A-sublattice, leading to the localization of oxygen vacancies in certain planes and the formation of a tetragonal superstructure $a_p \times a_p \times 2a_p$ for Ln = La, Pr, Nd (space group *P*4/*mmm*) and $2a_p \times 2a_p \times 4a_p$ for Ln = Sm, Gd, Dy, Y, Ho (space group *I*4/*mmm*) [26, 30, 33–36]. An increase in temperature leads to the destruction of superstructural ordering, and the phase transition temperature depends on the Ln/Sr ratio [26, 34–37]. For example, in air the transition from an ordered $2a_p \times 2a_p \times 4a_p$ superstructure to a disordered cubic one with statistically distributed Ln and Sr cations in the A-sublattice in $Gd_{0.2}Sr_{0.8}CoO_{3-\delta}$ is completed at 1363 K [36], which is in good agreement with the results in [37]. A similar structural transition in $Gd_{0.1}Sr_{0.9}CoO_{3-\delta}$ in air occurs at 1263 K [38]. A slightly different interpretation, although similar from the crystallographic point of view of the formation of an ordered arrangement of cations in the A-sublattice with the formation of a tetragonal cell, was given by Istomin et al. [39].

Oxygen nonstoichiometry in the $Ln_{1-x}Sr_xCoO_{3-\delta}$ (Ln = La–Gd) oxides changes slightly with decreasing radius of the lanthanide ion and increases significantly

with increasing strontium concentration in the samples [7, 26, 28, 30, 32, 37, 40]. It should also be noted that the oxygen content, along with the Ln/Sr ratio, significantly determines the formation of a superstructure in cobaltites [32, 41].

The introduction of iron into the cobalt sublattice in $Ln_{1-x}Sr_xCoO_{3-\delta}$ has a noticeable effect on the crystal structure and the entire set of physicochemical properties of the $Ln_{1-x}Sr_xCo_{1-y}Fe_yO_{3-\delta}$ (Ln = La–Gd) oxides [42–50]. Information on the structure and properties of solid solutions based on $GdCoO_3$ with simultaneous substitution in the A- and B-sublattices is scarce. It is known that cobaltites $Gd_{0.8}Sr_{0.2}Co_{1-y}Fe_yO_{3-\delta}$ ($0.0 \le y \le 1.0$) crystallize in an orthorhombic perovskite-like structure (space group *Pbnm*), and an increase in the iron concentration in the samples leads to a decrease in the thermal expansion coefficients and electrical conductivity [42, 43, 49]. This work is devoted to the study of phase relations in the quasi-quaternary $GdCoO_3$–$SrCoO_{3-\delta}$–$SrFeO_{3-\delta}$–$GdFeO_3$ system at 1373 K in air and influence of the substitution value on the homogeneity range, crystal structure and oxygen nonstoichiometry of $Gd_{1-x}Sr_xCo_{1-y}Fe_yO_{3-\delta}$ complex oxides.

EXPERIMENTAL

The synthesis of samples was carried out using glycerol-nitrate technique, described earlier in [45, 50]. The starting components were gadolinium oxide Gd_2O_3 (99.99%), strontium carbonate $SrCO_3$ (high purity grade), pre-calcined to remove adsorbed moisture and gases at 1373 K for 12 h and 773 K for 5 h, respectively, iron oxalate $FeC_2O_4{\cdot}2H_2O$ (analytical grade) and metal cobalt Co, obtained by reduction from cobalt oxide Co_3O_4 (analytical grade) at 673–873 K in a hydrogen flow. Final annealing was carried out at 1373 K in air for 60–80 h with intermediate grinding in ethyl alcohol after 12–15 h. The samples were quenched in air from 1373 K to room temperature by removing crucibles with a volume of <1 mL from a heated furnace onto a massive copper plate (cooling rate ~400–500 deg/min).

The phase composition of the studied samples was determined by X-ray powder diffraction using a Shimadzu XRD 7000 diffractometer with CuK_α radiation (λ = 1.5418 Å) using a pyrolytic graphite monochromator (angle range $10° \le 2\theta \le 80°$, step 0.02°, exposure at point 2 s). The structural parameters were refined using the Rietveld full-profile analysis method in the Fullprof-2011 software.

High-temperature XRD (HT-XRD) studies were carried out using an Inel Equinox 3000 diffractometer equipped with an HTK 16N high-temperature chamber (Anton Paar). Heating and cooling of the sample to a required temperature was performed at a rate of 100 K/h. The accuracy of temperature maintenance was ± 0.1 K.

The oxygen content in the oxides and its change with temperature were determined by thermogravimetric analysis. Measurements of temperature dependences were carried out using a thermal analyzer STA 409 PC Luxx in dynamic mode with a heating/cooling rate of 2 K/min in the temperature range 298–1373 K in air. The absolute value of oxygen content in oxides was determined by a complete reduction of samples with hydrogen (10% N_2 + 90% H_2) at 1423 K in a thermogravimetric cell to oxides Gd_2O_3, SrO and metallic cobalt Co and iron Fe. The phase composition of the reduced samples was controlled by X-ray powder diffraction.

RESULTS AND DISCUSSION

To study phase equilibria in the $GdCoO_3$–$SrCoO_{3-\delta}$–$SrFeO_{3-\delta}$–$GdFeO_3$ system 52 samples with various ratios of metal components were prepared at 1373 K in air using glycerol-nitrate technique.

Crystal Structure of $Gd_{1-x}Sr_xCo_{1-y}Fe_yO_{3-\delta}$ Oxides

Using X-ray powder diffraction, it was established that the homogeneity ranges and crystal structure of the $Gd_{1-x}Sr_xCo_{1-y}Fe_yO_{3-\delta}$ solid solutions depend significantly on the concentration of introduced strontium (x) and iron (y).

X-ray powder diffraction patterns of single-phase $Gd_{1-x}Sr_xCo_{1-y}Fe_yO_{3-\delta}$ oxides with $x = 0.0$ and $0.0 \le y \le 1.0$, $x = 0.1$ and $0.4 \le y \le 1.0$ and $x = 0.2$ and $y = 0.9$ quenched from 1373 K in air, similar to unsubstituted $GdMeO_3$ (Me = Fe, Co), were indexed within an orthorhombically distorted perovskite-like cell (space group *Pbnm*). Figure 1 shows, as an example, diffraction patterns of $Gd_{1-x}Sr_xCo_{0.2}Fe_{0.8}O_{3-\delta}$ with x = 0.0 and 0.1, refined using the Rietveld full-profile analysis. The refined unit cell parameters of $Gd_{1-x}Sr_xCo_{1-y}Fe_yO_{3-\delta}$ (x = 0.0; 0.1) are listed in Table 1. The linear increase in the unit cell parameters and unit cell volume for $Gd_{1-x}Sr_xCo_{1-y}Fe_yO_{3-\delta}$ (x = 0.0; 0.1) with increasing iron content (Fig. 2) corresponds to a larger radius of iron ions ($(r^{3+}_{Fe}/^{4+}_{Fe}$(HS) = 0.645/0.585 Å, CN = 6) compared to the radius of cobalt ions ($r^{3+}_{Co}/^{4+}_{Co}$ (HS) = 0.61/0.53 Å, CN = 6) [51].

The homogeneity range of $Gd_{1-x}Sr_xCo_{1-y}Fe_yO_{3-\delta}$ solid solutions with an orthorhombic structure is significantly smaller than that determined for similar oxides in the Nd-containing system $Nd_{1-x}Sr_xCo_{1-y}Fe_yO_{3-\delta}$ [45]. This can be explained by the larger difference in radii of gadolinium (r^{3+}_{Gd} = 1.107 Å) and strontium (r^{2+}_{Sr} = 1.44 Å) compared to the difference in radii between neodymium (r^{3+}_{Nd} = 1.27 Å) and strontium [51], and as a result, the replacement of Gd by Sr from the side of $GdCoO_3$ does not occur at all [52], and from the $GdFeO_3$ side it is significantly less [53].

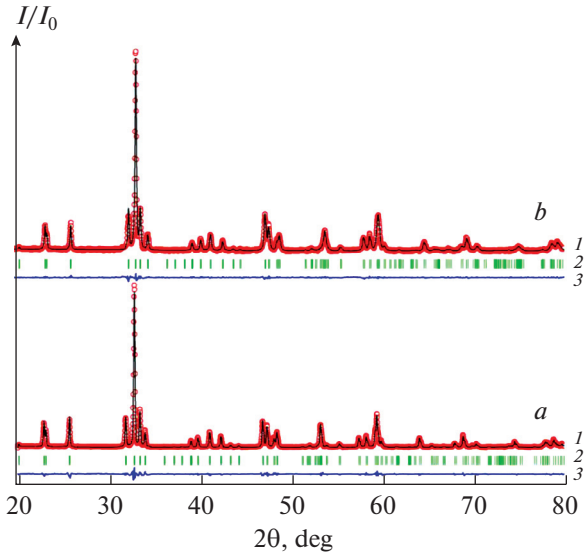

Fig. 1. X-ray powder diffraction data for $Gd_{1-x}Sr_xCo_{0.2}Fe_{0.8}O_{3-\delta}$ with $x = 0.0$ (*a*) and $x = 0.1$ (*b*), refined using the Rietveld method. Points show experimental data; (*1*) theoretical spectrum; (*2*) positions of peaks with allowed Miller indices (*hkl*); (*3*) difference between experimental data and theoretical curve.

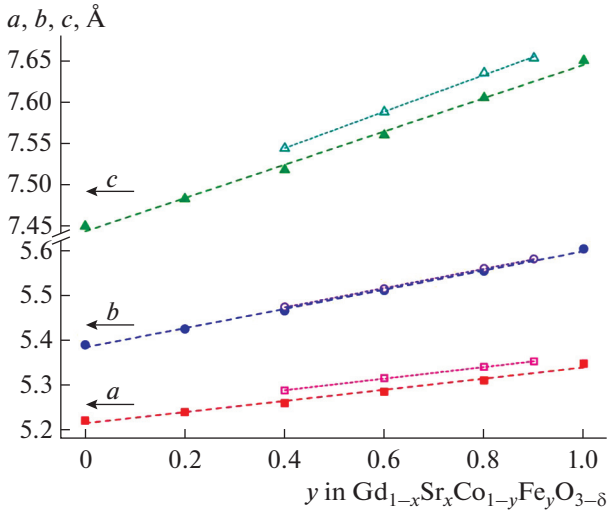

Fig. 2. Concentration dependences of the unit cell parameters of $Gd_{1-x}Sr_xCo_{1-y}Fe_yO_{3-\delta}$ solid solutions: with $x = 0.0$ and $0.0 \le y \le 1.0$ closed symbols, and with $x = 0.1$ and $0.4 \le y \le 0.9$ open symbols.

An increase in the concentration of strontium, which replaces gadolinium in $Gd_{1-x}Sr_xCo_{1-y}Fe_yO_{3-\delta}$ up to $x = 0.6$, again leads to the formation of single-phase oxides and a change in their crystallographic symmetry. Sr-enriched cobaltites $Gd_{1-x}Sr_xCo_{1-y}Fe_yO_{3-\delta}$ with $0.6 \le x \le 0.9$, depending on the iron content, have a tetragonal (space group $I4/mmm$) or cubic unit cell (space group $Pm\bar{3}m$). In the tetragonal ordered $2a_p \times 2a_p \times 4a_p$ structure, REE and strontium cations are distributed over three nonequivalent positions: A1 is completely occupied by REE ions, A2 occupied by strontium ions, and both REE and Sr are located in A3 positions [26, 38, 54]. Structural transitions in $Gd_{1-x}Sr_xCo_{1-y}Fe_yO_{3-\delta}$ with $x = 0.8$ and 0.9 were described in detail in our previous work [55].

The X-ray powder diffraction patterns of the $Gd_{1-x}Sr_xCo_{1-y}Fe_yO_{3-\delta}$ oxides with $0.6 \le x \le 0.7$ and $0.1 \le y \le 0.5$, quenched at 1373 K in air, similar to iron-free cobaltites $Gd_{1-x}Sr_xCoO_{3-\delta}$ ($0.6 \le x \le 0.8$) [26, 30, 37, 39, 52] contain superstructure reflections at scattering angles of $2\theta \approx 21°$ ($d \approx 4.26$ Å, $hkl = 103$) and $2\theta \approx 39°$ ($d \approx 2.29$ Å, $hkl = 215$), indicating the formation of a tetragonal supercells $2a_p \times 2a_p \times 4a_p$ (where a_p is the unit cell parameter of the basic perovskite). According to electron diffraction data [26, 30, 33, 39], the superstructure ($2a_p \times 2a_p \times 4a_p$) is formed by ordering of Gd and Sr cations in the A sublattice and the accompanying ordered arrangement of oxygen vacancies.

Table 1. Unit cells parameters of $Gd_{1-x}Sr_xCo_{1-y}Fe_yO_{3-\delta}$ oxides ($x = 0.0$; 0.1) quenched from 1373 K in air (space group *Pbnm*)

x	*y*	*a*, Å	*b*, Å	*c*, Å	*V*, Å^3	$c/\sqrt{2}$, Å	*R*-factors, %		
							R_{Br}	R_f	R_p
0.0	0.0	5.223(1)	5.391(1)	7.450(1)	209.77(1)	5.267	1.57	1.46	9.68
	0.2	5.242(1)	5.426(1)	7.483(1)	212.84(1)	5.291	2.80	3.11	10.10
	0.4	5.262(1)	5.466(1)	7.518(1)	216.23(2)	5.316	3.11	3.18	11.10
	0.6	5.287(1)	5.511(1)	7.560(1)	220.27(1)	5.345	2.99	3.23	9.21
	0.8	5.312(1)	5.554(1)	7.605(1)	224.37(1)	5.377	3.03	2.64	8.71
	1.0	5.349(1)	5.603(1)	7.666(1)	229.27(1)	5.409	1.26	1.33	8.42
0.1	0.4	5.290(1)	5.475(1)	7.544(1)	218.49(1)	5.334	6.04	5.70	6.08
	0.6	5.317(1)	5.515(1)	7.588(1)	222.50(2)	5.365	5.35	4.76	7.01
	0.8	5.342(1)	5.560(1)	7.635(1)	226.77(1)	5.398	6.32	5.38	5.80
	0.9	5.354(1)	5.581(1)	7.653(1)	228.68(1)	5.411	6.27	5.16	7.14

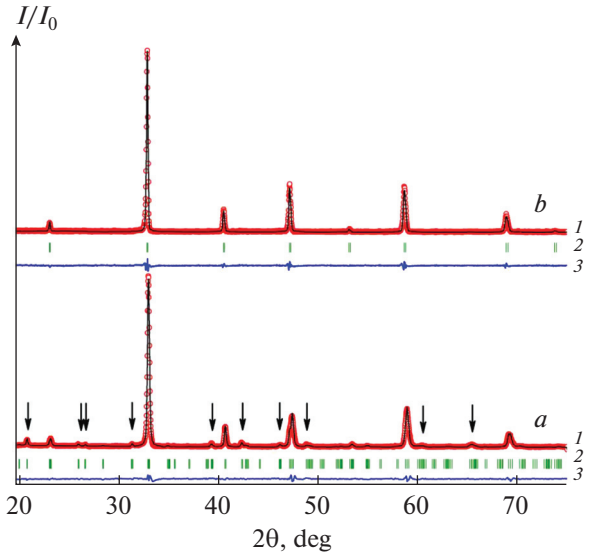

Fig. 3. X-ray powder diffraction data for $Gd_{0.3}Sr_{0.7}Co_{1-y}Fe_yO_{3-\delta}$ with $y = 0.2$ (*a*) and $y = 0.7$ (*b*), refined using the Rietveld method. Points show experimental data; (*1*) theoretical spectrum; (*2*) positions of peaks with allowed Miller indices (*hkl*); (*3*) difference between experimental data and theoretical curve. Arrows indicate superstructural reflections for the tetragonal cell $2a_p \times 2a_p \times 4a_p$.

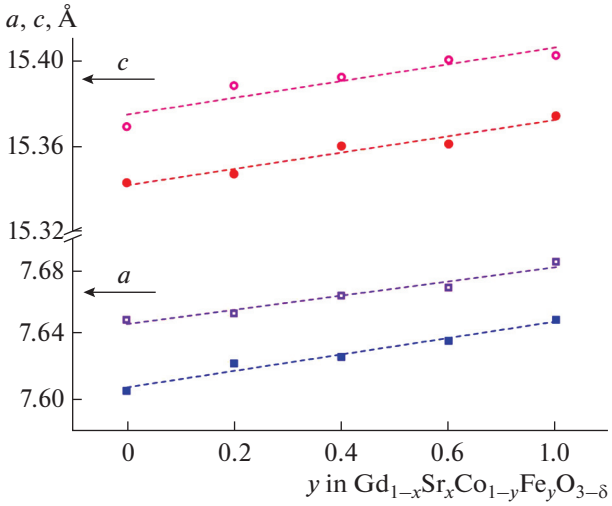

Fig. 4. Unit cell parameters versus composition for the $Gd_{1-x}Sr_xCo_{1-y}Fe_yO_{3-\delta}$ solid solution with $x = 0.6$ (closed symbols) and $x = 0.7$ (open symbols).

X-ray powder diffraction patterns of the $Gd_{1-x}Sr_xCo_{1-y}Fe_yO_{3-\delta}$ oxides with $0.6 \le x \le 0.7$ and $0.1 \le y \le 0.5$ were indexed in the tetragonal cell $2a_p \times 2a_p \times 4a_p$ (space group *I*4/*mmm*). Figure 3a, as an example, shows a typical X-ray powder diffraction pattern of $Gd_{0.3}Sr_{0.7}Co_{0.8}Fe_{0.2}O_{3-\delta}$ cobaltite refined by the Rietveld full-profile method. The structural parameters for $Gd_{1-x}Sr_xCo_{1-y}Fe_yO_{3-\delta}$ ($0.6 \le x \le 0.7$ and $0.1 \le y \le 0.5$) oxides refined by the Rietveld method are presented in Tables 2 and 3. The unit cell parameters and atomic coordinates for the $Gd_{0.2}Sr_{0.8}Co_{1-y}Fe_yO_{3-\delta}$ ($0.1 \le y \le 0.5$) solid solutions with a tetragonal structure are given in [55]. Substitution of Gd^{3+} (r = 1.107 Å) with larger Sr^{2+} cations (r = 1.44 Å) [51] and an increase in the content of iron replacing cobalt in $Gd_{1-x}Sr_xCo_{1-y}Fe_yO_{3-\delta}$ ($0.6 \le x \le 0.7$) from $y = 0.1$ to $y = 0.5$ lead to an increase in the unit cell parameters and volume, which is caused by the size effect (Fig. 4).

One of the most important factors in the formation of a superstructure with an ordered arrangement of cations in A-positions is the Gd/Sr ratio [26, 54], therefore, the replacement of Co by Fe, which is similar in many properties, does not initially affect the type of structure. However, along with the ordering of cations, the ordering of oxygen vacancies also plays an important role in the formation of the superstructure,

Table 2. Unit cells parameters of $Gd_{1-x}Sr_xCo_{1-y}Fe_yO_{3-\delta}$ solid solutions ($0.6 \le x \le 0.7$ and $0.1 \le y \le 0.5$) quenched from 1373 K in air (space group *I*4/*mmm*)

x	*y*	*a*, Å	*c*, Å	*V*, Å	*R*-factors, %		
					R_{Br}	R_f	R_p
0.7	0.1	7.650(1)	15.369(1)	899.55(2)	5.93	8.47	6.59
	0.2	7.654(1)	15.388(1)	901.59(2)	5.14	8.47	5.73
	0.3	7.665(1)	15.392(1)	904.38(1)	6.67	8.87	8.81
	0.4	7.670(1)	15.400(1)	906.15(3)	8.52	10.3	7.18
	0.5	7.686(1)	15.402(1)	910.09(2)	4.96	8.11	6.86
0.6	0.1	7.606(1)	15.343(1)	887.63(2)	6.50	10.4	11.38
	0.2	7.623(1)	15.347(1)	891.83(1)	6.90	11.7	13.70
	0.3	7.627(1)	15.360(1)	893.52(1)	8.6	9.7	10.38
	0.4	7.637(1)	15.361(1)	895.93(2)	7.7	8.0	10.40
	0.5	7.650(1)	15.374(1)	899.72(3)	9.3	11.3	11.47

Table 3. Atomic coordinates for $Gd_{0.3}Sr_{0.7}Co_{0.8}Fe_{0.2}O_{3-\delta}$ refined by the Rietveld method

Atom	*x*	*y*	*z*
Co(1)/Fe(1)	0.252(1)	0.252(1)	0
Co(2)/Fe(2)	0.250	0.250	0.250
Gd(1)	0	0	0.143(1)
Sr(2)	0	0	0.624(1)
Sr(3)/Gd(3)	0	0.5	0.131(3)
O(1)	0.225(1)	0.225(1)	0.116(1)
O(2)	0.271(1)	0	0
O(3)	0.216(3)	0.5	0
O(4)	0	0.252(3)	0.269(1)

and the introduction of iron ions, although not to the same extent as the replacement of Gd by Sr, still changes the oxygen content. An increase in the iron content in the $Gd_{1-x}Sr_xCo_{1-y}Fe_yO_{3-\delta}$ oxides with $0.6 \le x \le 0.7$ up to $y = 0.6$ leads to a transition from a tetragonal superstructure, with ordered Gd and Sr cations in the A-sublattice, to a cubic structure, with statistically distributed cations. X-ray powder diffraction patterns of the $Gd_{1-x}Sr_xCo_{1-y}Fe_yO_{3-\delta}$ oxides with $0.6 \le x \le 0.7$ and $0.6 \le y \le 0.9$, like those for the $Gd_{1-x}Sr_xFeO_{3-\delta}$ ferrites, were indexed in an ideal cubic structure (space group $Pm\bar{3}m$) [53]. Figure 3b, as an example, shows the X-ray powder diffraction pattern of cubic $Gd_{0.3}Sr_{0.7}Co_{0.3}Fe_{0.7}O_{3-\delta}$, refined by the Rietveld full-profile method. The structural parameters of $Gd_{1-x}Sr_xCo_{1-y}Fe_yO_{3-\delta}$ solid solutions with a cubic structure are listed in Table 4.

To compare the unit cell parameters of the $Gd_{1-x}Sr_xCo_{1-y}Fe_yO_{3-\delta}$ oxides with $x = 0.6$ and 0.7 over the entire concentration range ($0.1 \le y \le 0.9$), the parameters of the tetragonal supercell were recalculated to the pseudocubic one using the formula:

$$a_{\text{cubic}} = (V/z)^{1/3}, \quad (1)$$

where V is a volume of tetragonal supercell, z is the number of formula units (for $2a_p \times 2a_p \times 4a_p$ supercells $z = 16$). It can be seen that the dependence of the pseudocubic cell parameters (a_{cubic}) for the $Gd_{1-x}Sr_xCo_{1-y}Fe_yO_{3-\delta}$ oxides ($x = 0.6$ and 0.7) versus iron concentration (Fig. 5) exhibits a discontinuity in the composition range $0.5 \le y \le 0.6$ corresponding to the "order–disorder"-type structural transition, similar to that reported for cobaltites $Gd_{1-x}Sr_xCoO_{3-\delta}$ with increasing strontium content [37].

The X-ray powder diffraction patterns of samples with the nominal composition of $Gd_{1-x}Sr_xCo_{1-y}Fe_yO_{3-\delta}$ with $0.2 \le x \le 0.5$ and $0.2 \le y \le 0.8$ contained reflections of two types of solid solutions with orthorhombic (space group *Pbnm*) and cubic (space group $Pm\bar{3}m$) structures.

Oxygen Nonstoichiometry in $Gd_{1-x}Sr_xCo_{1-y}Fe_yO_{3-\delta}$ Oxides

The temperature dependences of the oxygen content in $Gd_{1-x}Sr_xCo_{0.3}Fe_{0.7}O_{3-\delta}$ solid solutions with $0.6 \le x \le 0.9$ are shown in Fig. 6. It can be seen that oxygen content in the samples noticeably decreases with increasing strontium concentration (Table 5). Heterovalent substitution of strontium for gadolinium leads to the formation of acceptor-type defects Sr'_{Gd}. Compensation for the excess negative charge in the structure occurs through the formation of an equivalent number of positively charged oxygen vacancies ($V_O^{\bullet\bullet}$) and holes ($h^{\bullet}$) localized on 3*d* transition metal ions. With increasing strontium content, the average oxidation state (Z) of 3*d* transition metal ions changes slightly from 3.02+ for $x = 0.6$ to 3.08 + for $x = 0.9$ at 1373 K ($\Delta Z = 0.06$) compared to the change in oxygen content from 2.71 for $x = 0.6$ to 2.59 for $x = 0.9$ at 1373 K ($\Delta(3 - \delta) = 0.12$, which corresponds to charge compensation $\Delta Z = 0.24$) (see Table 5). Thus, the lability of the oxygen sublattice [56] leads to the formation of solid solutions within a fairly wide range, since the sta-

Table 4. Structural parameters of $Gd_{1-x}Sr_xCo_{1-y}Fe_yO_{3-\delta}$ oxides quenched from 1373 K in air

Space group *Pm*-3*m*: Gd/Sr (0.5; 0.5; 0.5); Fe/Co (0; 0; 0); O (0.5; 0; 0)

x	*y*	*a*, Å	*V*, Å^3	$d_{\text{Fe/Co–O}}$, Å	$d_{\text{Gd/Sr–O}}$, Å	$d_{\text{Gd/Sr–Fe/Co}}$, Å	*R*-factors, %		
							R_{Br}	R_{f}	R_{p}
0.7	0.6	3.843(1)	56.78(1)	1.921(1)	2.717(1)	3.328(1)	3.93	4.37	7.39
	0.7	3.848(1)	56.98(1)	1.924(1)	2.722(1)	3.333(1)	2.73	2.11	7.23
	0.8	3.852(1)	57.16(1)	1.924(1)	2.722(1)	3.334(1)	4.48	2.93	8.33
	0.9	3.860(1)	57.51(1)	1.930(1)	2.729(1)	3.342(1)	4.53	4.40	8.97
0.6	0.6	3.833(1)	56.33(1)	1.916(1)	2.710(1)	3.320(1)	5.7	4.75	14.2
	0.7	3.838(1)	56.55(1)	1.919(1)	2.714(1)	3.324(1)	8.75	8.72	13.6
	0.8	3.846(1)	56.92(1)	1.922(1)	2.719(1)	3.330(1)	3.16	4.76	10.2
	0.9	3.852(1)	57.18(1)	1.926(1)	2.724(1)	3.336(1)	4.90	5.31	12.1

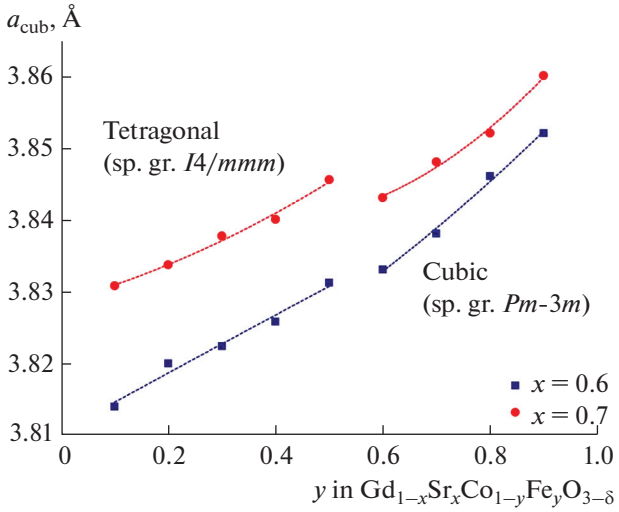

Fig. 5. The unit cell parameters of a pseudo-cubic cell versus composition for the $Gd_{1-x}Sr_xCo_{1-y}Fe_yO_{3-\delta}$ solid solution.

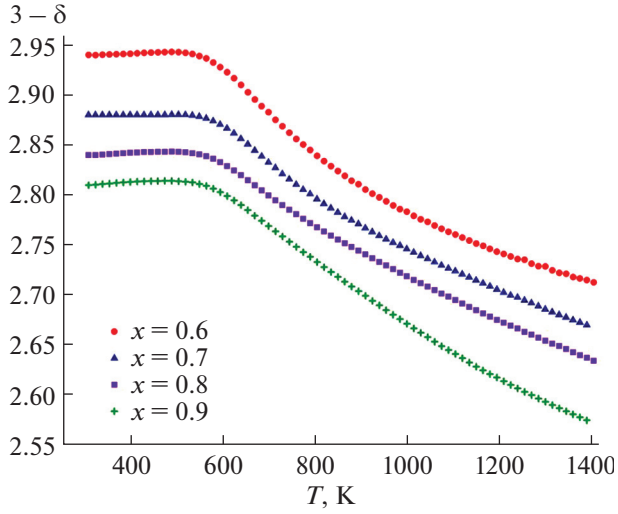

Fig. 6. Oxygen content in the $Gd_{1-x}Sr_xCo_{0.3}Fe_{0.7}O_{3-\delta}$ oxides ($0.6 \le x \le 0.9$) vs. temperature in air.

bility of oxides with a perovskite structure is largely determined by the thermodynamically favorable oxidation state of 3*d* metals at certain T, Po_2 [57], and charge compensation in $Gd_{1-x}Sr_xCo_{0.3}Fe_{0.7}O_{3-\delta}$ within the studied temperature range in air is determined mainly due to the formation of oxygen vacancies ($V_O^{\cdot\cdot}$).

In a case when the average oxidation state of 3*d* metals is above 3+, the more electropositive iron ions will predominantly have oxidation state of 4+ (electronegativity of Fe = 1.64; electronegativity of Co = 1.7 [58]). In other words, the equilibrium in the reaction $Fe^{4+} + Co^{3+} = Fe^{3+} + Co^{4+}$ is significantly shifted to the left-hand side. Using the electroneutrality condition and experimentally determined values of oxygen content, the formulas of solid solutions $Gd_{1-x}Sr_xCo_{0.3}Fe_{0.7}O_{3-\delta}$ can be represented as follows:

$T = 298$ K, air

$Gd_{0.4}Sr_{0.6}Co^{3+}_{0.3}Fe^{3+}_{0.22}Fe^{4+}_{0.48}O_{2.94}$

$Gd_{0.3}Sr_{0.7}Co^{3+}_{0.3}Fe^{3+}_{0.24}Fe^{4+}_{0.46}O_{2.88}$

$Gd_{0.2}Sr_{0.8}Co^{3+}_{0.3}Fe^{3+}_{0.22}Fe^{4+}_{0.48}O_{2.84}$

$Gd_{0.1}Sr_{0.9}Co^{3+}_{0.3}Fe^{3+}_{0.18}Fe^{4+}_{0.52}O_{2.81}$

$T = 1373$ K, air

$Gd_{0.4}Sr_{0.6}Co^{3+}_{0.3}Fe^{3+}_{0.68}Fe^{4+}_{0.02}O_{2.71}$

$Gd_{0.3}Sr_{0.7}Co^{3+}_{0.3}Fe^{3+}_{0.66}Fe^{4+}_{0.04}O_{2.67}$

$Gd_{0.2}Sr_{0.8}Co^{3+}_{0.3}Fe^{3+}_{0.62}Fe^{4+}_{0.08}O_{2.64}$

$Gd_{0.1}Sr_{0.9}Co^{3+}_{0.3}Fe^{3+}_{0.64}Fe^{4+}_{0.06}O_{2.59}$

It can be seen that although the charge compensation with increasing strontium concentration is carried out mainly due to the release of oxygen from the lattice which is accompanied with the formation of oxygen vacancies, the fraction of Fe^{4+} ions also increase slightly. Similar results were obtained earlier for perovskite-like oxides of the composition $Ln_{1-x}Sr_xCo_{1-y}Fe_yO_{3-\delta}$ (Ln = La, Nd) [44, 45, 50].

Phase Diagram of the $GdCoO_3$–$SrCoO_{3-\delta}$–$SrFeO_{3-\delta}$–$GdFeO_3$ System

The phase diagrams of quasi-binary systems $GdCoO_3$–$SrCoO_{3-\delta}$, $GdFeO_3$–$SrFeO_{3-\delta}$, $SrCoO_{3-\delta}$–$SrFeO_{3-\delta}$ necessary for constructing the phase diagram of the quasi-quaternary system $GdCoO_3$–$SrCoO_{3-\delta}$–$SrFeO_{3-\delta}$–$GdFeO_3$ at 1373 K in air, were studied in detail earlier in [52, 53, 59]. The homogeneity range limits and the type of crystal structure for the oxides formed in these systems at 1373 K in air are given in Table 6.

The X-ray powder diffraction pattern of $SrCoO_{3-\delta}$ cobaltite quenched from 1373 K in air was indexed within an orthorhombic cell with unit cell parameters $a = 5.615(1)$ Å, $b = 15.580(1)$ Å, $c = 5.563(1)$ Å (space group *Pnma*) [59], which is in good agreement with the results reported in [60]. However, according to HT-XRD data [52], $SrCoO_{3-\delta}$ at 1373 K in air crystal-

Table 5. Oxygen content and average oxidation state of 3*d* transition metals in $Gd_{1-x}Sr_xCo_{0.3}Fe_{0.7}O_{3-\delta}$ in air

x	T, K	$3-\delta$	Average oxidation state of 3*d* metals
0.6	298	2.94 ± 0.01	3.48
	1373	2.71 ± 0.01	3.02
0.7	298	2.88 ± 0.01	3.46
	1373	2.67 ± 0.01	3.04
0.8	298	2.84 ± 0.01	3.48
	1373	2.64 ± 0.01	3.08
0.9	298	2.81 ± 0.01	3.52
	1373	2.59 ± 0.01	3.08

lizes in an ideal cubic structure (space group $Pm\bar{3}m$), and the quenching rate after removing the sample to room temperature is insufficient to preserve the structure. To clarify the homogeneity range of the $SrFe_{1-x}Co_xO_{3-\delta}$ solid solution, HT-XRD measurement of the $SrFe_{0.2}Co_{0.8}O_{3-\delta}$ complex oxide was additionally performed. According to the obtained results cobaltite $SrFe_{0.2}Co_{0.8}O_{3-\delta}$ at 1373 K in air possesses a cubic perovskite structure with the unit cell parameter $a = 3.984(1)$ Å (space group $Pm\bar{3}m$). Thus, in the $SrCoO_{3-\delta}$–$SrFeO_{3-\delta}$ system under experimental conditions studied a series of solid solutions $SrFe_{1-x}Co_xO_{3-\delta}$ with a tetragonal structure is formed inside the range $0.0 \le x < 0.3$, and another one with a cubic structure inside the range $0.3 \le x \le 1.0$, which is consistent with the data reported in [61].

Taking into account the X-ray powder diffraction results of all studied samples quenched to room temperature, a phase diagram for the $GdCoO_3$–$SrCoO_{3-\delta}$–$SrFeO_{3-\delta}$–$GdFeO_3$ system at 1373 K in air was constructed (Fig. 7). The phase diagram shows the stability regions of $Gd_{1-x}Sr_xCo_{1-y}Fe_yO_{3-\delta}$ solid solutions with orthorhombic (space group *Pbnm*), tetragonal (space group *I*4/*mmm*) and cubic (space group $Pm\bar{3}m$) structure. The structural transition of "order⇔disorder"-type for the $Gd_{1-x}Sr_xCo_{1-y}Fe_yO_{3-\delta}$ oxides with $0.6 \le x \le 0.8$ at $y > 0.5$ refers to the second order phase transitions, which boundary is extended and cannot be attributed to fixed parameters, thus in the phase diagram it is shown by a dash line. The shaded fields correspond to the coexistence of two types of solid solutions.

CONCLUSIONS

It has been shown that the crystal structure of $Gd_{1-x}Sr_xCo_{1-y}Fe_yO_{3-\delta}$ solid solutions depends significantly on the concentration of introduced strontium and iron. At low strontium contents, $Gd_{1-x}Sr_xCo_{1-y}Fe_yO_{3-\delta}$ complex oxides ($x = 0.0$ and $0.0 \le y \le 1.0$; $x = 0.1$ and $0.4 \le y \le 1.0$; $x = 0.2$ and $y = 0.9$) have an orthorhombically distorted perovskite structure (space group *Pbnm*); strontium-enriched $Gd_{1-x}Sr_xCo_{1-y}Fe_yO_{3-\delta}$ oxides with $0.6 \le x \le 0.8$ and low iron content of $0.1 \le y \le 0.5$ crystallize in a tetragonal supercell $2a_p \times 2a_p \times 4a_p$ (space group *I*4/*mmm*) with ordered Gd and Sr cations in the A-sublattice, and oxides with $0.6 \le x \le 0.8$ and high iron content $0.6 \le y \le 0.9$ crystallize in a cubic cell with statistically distributed cations. The increase in the unit cell parameters of the $Gd_{1-x}Sr_xCo_{1-y}Fe_yO_{3-\delta}$ oxides with increasing strontium and/or iron content is associated with the size

Table 6. Homogeneity ranges and crystal structure of solid solutions formed in quasi-binary systems at 1373 K in air

System	Composition of solid solution		Crystal system (space group)	Ref.
$GdCoO_3$–$SrCoO_{3-\delta}$	$Sr_{1-x}Gd_xCoO_{3-\delta}$	$0.0 \le x \le 0.19$	Cubic ($Pm\bar{3}m$)	[52]
		$0.2 \le x \le 0.4$	Tetragonal (*I*4/*mmm*)	
		$1.0 \le x < 0.4$	$GdCoO_{3-\delta} + Sr_{0.6}Gd_{0.4}CoO_{3-\delta}$	
$GdFeO_3$–$SrFeO_{3-\delta}$	$Sr_{1-x}Gd_xFeO_{3-\delta}$	$0.05 \le x \le 0.3$	Cubic ($Pm\bar{3}m$)	[53]
		$0.8 \le x \le 1.0$	Orthorhombic (*Pbnm*)	
$SrCoO_{3-\delta}$–$SrFeO_{3-\delta}$	$SrFe_{1-x}Co_xO_{3-\delta}$	$0.0 \le x < 0.3$	Tetragonal (*I*4/*mmm*)	[59]
		$0.3 \le x \le 0.7$	Cubic ($Pm\bar{3}m$)	
		$0.7 < x < 1.0$	$SrCoO_{3-\delta} + SrFe_{0.3}Co_{0.7}O_{3-\delta}$	
$GdCoO_3$–$GdFeO_3$	$GdCo_{1-y}Fe_yO_3$	$0.0 \le y \le 1.0$	Orthorhombic (*Pbnm*)	Present work

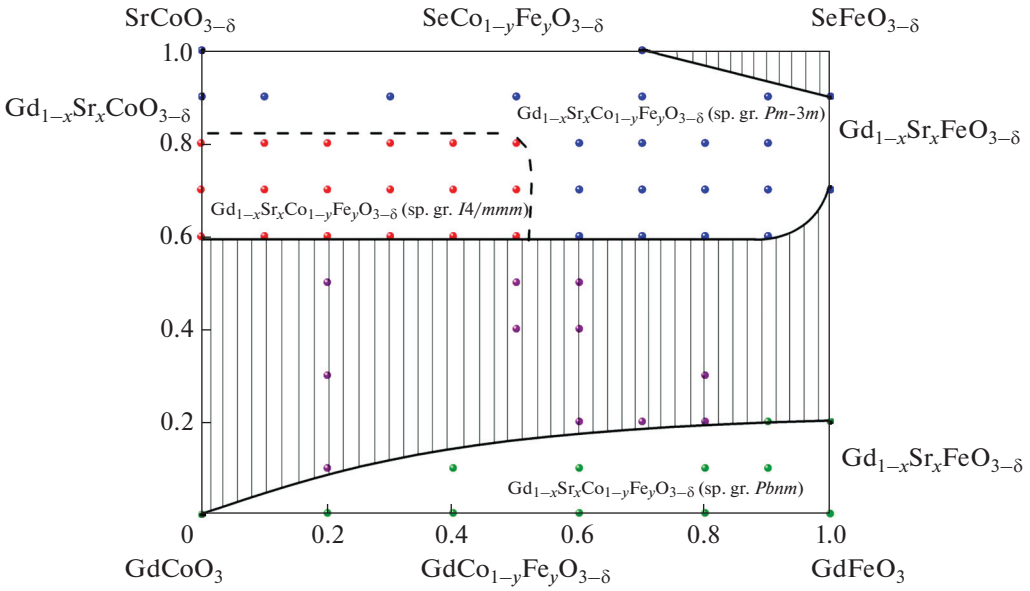

Fig. 7. Isobaric-isothermal phase diagram for the $GdCoO_3$–$SrCoO_{3-\delta}$–$SrFeO_{3-\delta}$–$GdFeO_3$ system at 1373 K in air. Green points correspond to the orthorhombic structure of $Gd_{1-x}Sr_xCo_{1-y}Fe_yO_{3-\delta}$ (space group *Pbnm*), blue points to the cubic structure (space group *Pm*-3*m*), red points to the tetragonal ordered structure (space group *I*4/*mmm*). Purple dots correspond to the two-phase region where orthorhombic and tetragonal (or cubic) structures coexist.

effect. The oxygen content in $Gd_{1-x}Sr_xCo_{1-y}Fe_yO_{3-\delta}$ cobaltites decreases with increasing temperature (which corresponds to more reducing conditions), increasing strontium concentration (representing the acceptor-type substituent Sr'_{Gd}) and, to a slightly lesser extent, with decreasing iron concentration (representing the donor-type substituent). An isobaric-isothermal section of the phase diagram of the $GdCoO_3$–$SrCoO_{3-\delta}$–$SrFeO_{3-\delta}$–$GdFeO_3$ system at 1373 K in air has been constructed.

FUNDING

The work was financially supported by the Ministry of Science and Higher Education of the Russian Federation (state registration number 123031300049-8).

CONFLICT OF INTEREST

The authors of this work declare that they have no conflicts of interest.

REFERENCES

1. A. I. Klyndyuk, Ya. Yu. Zhuravleva, N. N. Gundilovich, et al., Inorg. Mat. **59**, 86 (2023). https://doi.org/10.1134/S0020168523010089
2. T. L. Simonenko, N. P. Simonenko, E. P. Simonenko, et al., Russ. J. Inorg. Chem. **67**, 1495 (2022). https://doi.org/10.1134/S0036023622600939
3. A. I. Klyndyuk and Ya. Yu. Zhuravleva, Russ. J. Inorg. Chem. **67**, 2084 (2022). https://doi.org/10.1134/S0036023622601404
4. M. V. Kalinina, D. A. Dyuskina, I. G. Polyakova, et al., Glass Phys. Chem. **49**, 177 (2023). https://doi.org/10.1134/S1087659622601046
5. E. A. Chizhova, A. I. Klyndyuk, Ya. Yu. Zhuravleva, et al., Glass Phys. Chem. **49**, 57 (2023). https://doi.org/10.1134/S1087659622600910
6. H. Fan, Z. Liu, Y. Wu, et al., Int. J. Appl. Ceram. Technol. **21**, 289 (2023). https://doi.org/10.1111/ijac.14490
7. K. T. Lee and A. Manthiram, J. Electrochem. Soc. **153**, A794 (2006). https://doi.org/10.1149/1.2172572
8. K. T. Lee and A. Manthiram, J. Electrochem. Soc. **152**, A197 (2005). https://doi.org/10.1149/1.1828243
9. C. Rossignol, J. M. Ralph, J.-M. Bae, et al., Solid State Ionics **175**, 59 (2004). https://doi.org/10.1016/j.ssi.2004.09.021
10. Y. Takeda, H. Ueno, N. Imanishi, et al., Solid State Ionics **86–88**, 1187 (1996). https://doi.org/10.1016/0167-2738(96)00285-8
11. Q. Ni, H. Chen, L. Ge, et al., J. Power Sources **349**, 130 (2017). https://doi.org/10.1016/j.jpowsour.2017.03.037
12. X. Tong, S. Ovtar, K. Brodersen, et al., J. Power Sources **451**, 227742 (2020). https://doi.org/10.1016/j.jpowsour.2020.227742
13. R. K. Madathil and T. Norby, Solid State Sci. **124**, 106801 (2022). https://doi.org/10.1016/j.solidstatesciences.2021.106801
14. O. F. Kononchuk, A. N. Petrov, and V. A. Cherepanov, Inorg. Mater. **27**, 1662 (1991).

15. S. N. Vereshchagin, L. A. Solovyov, E. V. Rabchevskii, et al., Chem. Commun. **50**, 6112 (2014). https://doi.org/10.1039/c4cc00913d
16. C. Tealdi, IslamM. Saiful, C. Fisher, et al., Prog. Solid State Chem. **35**, 491 (2007). https://doi.org/10.1016/j.progsolidstchem.2007.01.015
17. X. Wang, K. Huang, W. Ma, et al., Chem.-Eur. J. **23**, 1093 (2017). https://doi.org/10.1002/chem.201604065
18. H. Liu, Y. Guo, R. Xie, et al., Sens. Actuat. B **246**, 164 (2017). https://doi.org/10.1016/j.snb.2017.02.072
19. J. He, J. Sunarso, J. Miao, et al., J. Hazard. Mater. **369**, 699 (2019). https://doi.org/10.1016/j.jhazmat.2019.02.070
20. T. Li, R. S. Jayathilake, D. D. Taylor, et al., Chem. Commun. **55**, 4929 (2019). https://doi.org/10.1039/C8CC09573F
21. V. A. Dudnikov, Y. S. Orlov, N. V. Kazak, et al., Ceram. Int. **45**, 5553 (2019). https://doi.org/10.1016/j.ceramint.2018.12.013
22. M. S. Reis, D. L. Rocco, VivasR. J. Caraballo, et al., J. Magn. Magn. Mater. **422**, 197 (2017). https://doi.org/10.1016/j.jmmm.2016.08.080
23. K. H. Ryu, K. S. Roh, S. J. Lee, et al., J. Solid State Chem. **105**, 550 (1993). https://doi.org/10.1006/jssc.1993.1247
24. L. Zhang, X. Li, F. Wang, et al., Mater. Res. Bull. **48**, 1088 (2013). https://doi.org/10.1016/j.materresbull.2012.11.105
25. P. T. Long, T. V. Manh, T. A. Ho, et al., Ceram. Int. **44**, 15542 (2018). https://doi.org/10.1016/j.ceramint.2018.05.216
26. M. James, D. Cassidy, D. J. Goossens, et al., J. Solid State Chem. **177**, 1886 (2004). https://doi.org/10.1016/j.jssc.2004.01.012
27. N. Alhokbany, S. Almotairi, J. Ahmed, et al., J. King Saud. Univer. Sci. **33**, 101419 (2021). https://doi.org/10.1016/j.jksus.2021.101419
28. A. N. Petrov, O. F. Kononchuk, A. V. Andreev, et al., Solid State Ionics **80**, 189 (1995). https://doi.org/10.1016/0167-2738(95)00114-l
29. V. A. Cherepanov, L. Ya. Gavrilova, L. Yu. Barkhatova, et al., Ionics **4**, 309 (1998). https://doi.org/10.1007/BF02375959
30. M. James, T. Tedesco, D. J. Cassidy, et al., Mater. Res. Bull. **40**, 990 (2005). https://doi.org/10.1016/j.materresbull.2005.02.020
31. S. Park, S. Choi, J. Shin, et al., J. Power Sources **210**, 172 (2012). https://doi.org/10.1016/j.jpowsour.2012.03.018
32. T. V. Aksenova, T. G. Efimova, O. I. Lebedev, et al., J. Solid State Chem. **248**, 183 (2017). https://doi.org/10.1016/j.jssc.2017.02.002
33. M. James, M. Avdeev, P. Barnes, et al., J. Solid State Chem. **180**, 2233 (2007). https://doi.org/10.1002/chin.200835004
34. V. A. Dudnikov, Y. S. Orlov, N. V. Kazak, et al., Ceram. Int. **44**, 10299 (2018). https://doi.org/10.1016/j.ceramint.2018.03.037
35. S. N. Vereshchagin, V. A. Dudnikov, N. N. Shishkina, et al., Thermochim. Acta **655**, 34 (2017). https://doi.org/10.1016/j.tca.2017.06.003
36. V. A. Dudnikov, Yu. S. Orlov, S. Yu. Gavrilkin, et al., J. Phys. Chem. **120**, 13443 (2016). https://doi.org/10.1021/acs.jpcc.6b04810
37. A. V. Maklakova, A. S. Baten'kova, M. A. Vlasova, et al., Solid State Sci. **110**, 106453 (2020). https://doi.org/10.1016/j.solidstatesciences.2020.106453
38. V. A. Dudnikov, N. V. Kazak, Y. S. Orlov, et al., J. Exp. Theor. Phys. **128**, 630 (2019). https://doi.org/10.1134/S1063776119020171
39. S. Y. Istomin, O. A. Drozhzhin, and G. Svensson, Solid State Sci. **6**, 539 (2004). . https://doi.org/10.1016/j.solidstatesciences.2004.03.029
40. A. N. Petrov, V. A. Cherepanov, O. F. Kononchuk, et al., J. Solid State Chem. **87**, 69 (1990). https://doi.org/10.1016/0022-4596(90)90066-7
41. M. James, L. Morales, K. Wallwork, et al., Physica B **385–386**, 199 (2006). https://doi.org/10.1016/j.physb.2006.05.244
42. L. Qiu, T. Ichikawa, A. Hirano, et al., Solid State Ionics **158**, 55 (2002). https://doi.org/10.1016/S0167-2738(02)00757-9
43. C. R. Dyck, G. Yu, and V. D. Krstic, Mat. Res. Soc. Symp. Proc. **801**, 114 (2003). https://doi.org/10.1557/PROC-801-BB3.4
44. T. V. Aksenova, V. A. Cherepanov, L. Ya. Gavrilova, et al., Prog. Solid State Chem. **35**, 175 (2007). https://doi.org/10.1016/j.progsolidstchem.2007.03.001
45. Sh. I. Elkalashy, A. R. Gilev, T. V. Aksenova, et al., Solid State Ionics **31**, 85 (2018). https://doi.org/10.1016/j.ssi.2017.12.028
46. Q. Xu, D. Huang, W. Chen, et al., J. Alloys Compd. **429**, 34 (2007). https://doi.org/10.1016/j.jallcom.2006.04.005
47. N. Dasgupta, R. Krishnamoorthy, and J. K. Thomas, Mater. Sci. Eng. **90**, 278 (2002). https://doi.org/10.1016/S0921-5107(02)00058-2
48. K. T. Lee and A. Manthiram, Solid State Ionics **176**, 1521 (2005). https://doi.org/10.1016/j.ssi.2005.05.002
49. F. Riza, Ch. Ftikos, F. Tietz, et al., J. Eur. Ceram. Soc. **21**, 1769 (2001). https://doi.org/10.1016/S0955-2219(01)00112-1
50. Sh. I. Elkalashy, T. V. Aksenova, A. S. Urusova, et al., Solid State Ionics **295**, 96 (2016). https://doi.org/10.1016/j.ssi.2016.08.005
51. R. D. Shannon, Acta Crystallogr. A **32**, 751 (1976). https://doi.org/10.1107/S0567739476001551
52. A. V. Maklakova, M. A. Vlasova, N. E. Volkova, et al., J. Alloys Compd. **883**, 160794 (2021). https://doi.org/10.1016/j.jallcom.2021.160794
53. L. V. Khvostova, N. E. Volkova, L. Ya. Gavrilova, et al., Mater. Today Comm. **29**, 102885 (2021). https://doi.org/10.1016/j.mtcomm.2021.102885
54. N. E. Volkova, A. V. Maklakova, L. Ya. Gavrilova, et al., Eur. J. Inorg. Chem. **2017**, 3285 (2017). https://doi.org/10.1002/ejic.201700321

55. T. V. Aksenova, D. K. Mysik, and V. A. Cherepanov, Catalysts **12**, 1344 (2022). https://doi.org/10.3390/catal12111344

56. E. V. Tsipis, E. N. Naumovich, M. V. Patrakeev, et al., J. Solid State Electrochem. **25**, 2777 (2021). https://doi.org/10.1007/s10008-021-05023-8

57. V. A. Cherepanov, L. Yu. Barkhatova, and A. N. Petrov, J. Phys. Chem. Solids **55**, 229 (1994). https://doi.org/10.1016/0022-3697(94)90137-6

58. J. I. Huheey, *Inorganic Chemistry* (Harper & Row, New York, 1983).

59. T. V. Aksenova, L. Ya. Gavrilova, and V. A. Cherepanov, J. Solid State Chem. **10**, 1480 (2008). https://doi.org/10.1016/j.jssc.2008.03.010

60. J. C. Grenier, L. Fournes, M. Pouchard, et al., Mater. Res. Bull. **21**, 441 (1986). https://doi.org/10.1016/0025-5408(86)90009-7

61. T. Takeda and H. Watanabe, J. Phys. Soc. Jpn. **33**, 973 (1972). https://doi.org/10.1143/JPSJ.33.973